

Article

Investigating Flood Impact on Crop Production under a Comprehensive and Spatially Explicit Risk Evaluation Framework

Xi Wang ¹, Zhanyan Liu ² and Huili Chen ^{3,*}

¹ College of Urban and Environmental Sciences, Peking University, No.5 Yiheyuan Road, Haidian District, Beijing 100871, China; pkuwangx@pku.edu.cn

² Handan Hydrology and Water Resources Survey Bureau of Hebei Province, Handan 056001, China; liuzhanyan2006@126.com

³ School of Architecture, Building and Civil Engineering, Loughborough University, Loughborough LE11 3TU, UK

* Correspondence: h.chen2@lboro.ac.uk

Abstract: Due to the projected increased frequency of occurrence of extreme flood events, it is becoming increasingly important to pay attention to agricultural flood management. The middle and lower reaches of the Yangtze River Basin (MLYRB), as one of the most important agricultural areas in the world, frequently suffer from the ravages of long-duration extreme flood events. Comprehensive flood risk evaluation can provide important support for effective management strategies by focusing on the combination of flood hazard and the consequences of flooding in areas exposed to the inundation. Previous satellite-based flood disturbance detection methods intended for use in single-cropping agricultural systems cannot be applied to the MLYRB with multi-cropping practices and long-duration flood events. Additionally, comprehensive agricultural flood risk evaluations traditionally neglect the characteristics of the impact of flooding with strong spatial and temporal variability. Thus, in this research, an integrated disturbance index (IDI) was developed to detect the impact of flood disturbance on crop growth, aiming to acquire a map of crop damage condition for a multi-cropping agricultural system with long-duration flood events that is spatially explicit and has a sufficiently high spatial resolution. A coupled hydrological and 2D hydraulic model parallelized using the GPU approach was employed to simulate flood flows, aiming at deriving sufficient meaningful detail at the local scale in terms of flood inundation patterns and processes over the whole natural watershed. Additionally, a spatial map of the combined effects of flood hazard and the consequences of flooding was used to investigate the relationship between flood characteristics and associated loss extent with the random forest model. The comprehensive evaluation framework was applied for the 2010 flood event in the MLYRB. The evaluation results indicate that the detection results based on IDI are consistent with the governmental statistics, the most hard-hit areas in related reports, and the spatial characteristics of river floods. The coupled hydrological–hydraulic model offers a clear picture of the flood characteristics over the whole basin, while simultaneously ensuring a sufficiently high spatial resolution. Our findings show that flood duration is the most important predictor in predicting crop damage extent.

Keywords: flooding; crop production; disturbance detection index; two-dimensional hydraulic model; spatial characteristics



Citation: Wang, X.; Liu, Z.; Chen, H. Investigating Flood Impact on Crop Production under a Comprehensive and Spatially Explicit Risk Evaluation Framework. *Agriculture* **2022**, *12*, 484. <https://doi.org/10.3390/agriculture12040484>

Academic Editor:
Tarendra Lakhankar

Received: 25 January 2022

Accepted: 29 March 2022

Published: 30 March 2022

Publisher's Note: MDPI stays neutral with regard to jurisdictional claims in published maps and institutional affiliations.



Copyright: © 2022 by the authors. Licensee MDPI, Basel, Switzerland. This article is an open access article distributed under the terms and conditions of the Creative Commons Attribution (CC BY) license (<https://creativecommons.org/licenses/by/4.0/>).

1. Introduction

Rainfall-induced flooding and accompanying waterlogging are agricultural disasters that occur frequently in many regions of the world and often cause remarkable damage to crop production [1]. Besides the direct rushing effect, the submergence creates complex abiotic stress in crops, including reduced light availability [2], oxygen depletion [3], and

altered chemical characteristics of soil [4]. The combination of all these physical and chemical alterations can substantially reduce crop stand and the growth and yield of crops. Under current climate conditions, the reduction in crop yields owing to excess rainfall events has been substantial, negatively influencing the grain supply and creating food security [5]. The intensification of the hydrological cycle due to climate warming is projected to alter the timing, magnitude, and frequency of extreme floods [6–8]. The accompanying crop damage created by flooding is likely to be greater under future climate conditions; consequently, the management of agricultural floods is expected to face more challenges.

As one of the countries worst affected by flooding, China frequently suffers from the ravages of extreme flood events. The Yangtze River is the longest river in China and the third in the world in terms of its length and river flow. It is responsible for approximately 70% of China's floods [9]. Historically, the Yangtze River Basin has been well known for its frequent flood events, especially in its middle and lower reaches. Heavy rainfall in the MLYRB due to strong and lengthy El Niño events brings about severe flooding and serious loss of property and life. Among the recent largest floods are those of 1870, 1931, 1954, 1998, and 2010. The 1954 flood event in the Yangtze River Basin inundated an area of 193,000 km², killed 33,169 people, and caused the displacement of 18,884,000 people [10]. The Yangtze River Basin is affected by the joint influence of the tropical and subtropical East Asian summer monsoons. Under the monsoonal climate, floods occur in the summer, especially during June and July, when slow-moving cold fronts meet the humid and steady subtropical air-mass and lead to excessive rainfall in the Yangtze River Basin [11]. These flood disasters not only have serious consequences but are characterized by a high water level and long duration (e.g., more than 70 days for the 1998 flood), especially in the MLYRB [12]. The upper reaches of the Yangtze River are basically mountainous terrain, and the middle and lower reaches are primarily a flattened floodplain. Large amounts of sediment (ca. 0.8×10^8 tons/a) are deposited in the middle reaches as a result of the decrease in slope from the upstream mountain valley to the downstream flattened meandering river [13]. Along with the continuous deposition of sediment and embankment construction, the current levee is 10–15 m higher than the outside areas along the networks, which makes the flood evolution more complicated [14]. Additionally, the effects of the “suspending river” lead to the surface of the floodplain being depressed and making it extremely prone to becoming waterlogged. The high frequency and long duration of flood disasters, in combination with poor water discharge, constitute a huge challenge to agricultural production in the MLYRB. This is why flood disasters are the most serious form of natural disaster in terms of agricultural production and account for 40% yield reductions in the MLYRB [15].

Worse yet, obvious climate change and huge landscape changes occur in the Yangtze River Basin. Some studies have investigated the statistical characteristics of historical extreme precipitation in the Yangtze River Basin [11,16–19]. A significant increasing trend in summer precipitation intensity over the MLYRB has been detected in the last 50 years. Furthermore, due to global warming, the return periods of extreme precipitation events are projected to become shorter in the MLYRB [20,21]. A significant increase in summer precipitation would lead to a higher possibility of the occurrence of flood hazards [22]. Besides abnormally extreme rainfall events, the Yangtze River Basin has experienced extensive landscape changes, including land use/cover changes (e.g., deforestation, urbanization, and soil erosion) [23,24], the shrinkage of large lakes in the floodplain of the Yangtze River Basin [25,26], and the construction of levees along riverbanks [12]. These landscape changes caused by human activity may create extra pressure on the environment, increasing the severity of major floods in the MLYRB [14,27,28]. Thus, the severity of this situation prompts us to select the MLYRB as our study area, aiming to more deeply understand the influence of flooding on crop production in order to cope with the projected more severe and frequent floods.

It is important to remember that the MLYRB is one of the most important agricultural areas in the world and is famous for being the “Land of Rice and Fish”. The warm and humid climate, abundant light and heat, and equal periods of rain and heat are beneficial to agricultural production. The cropping systems used in the MLYRB are double-cropping or triple-cropping in one year, with rape–rice–rice cropping primarily used in the southern region and wheat–rice cropping primarily used in the northern region [29]. The farming land is highly productive, and the crops planted are very diverse, with the major ones being rice, wheat, cotton, rape, and silkworm. Thus, the spatial distribution of crop types and crop rotations have obvious heterogeneity due to the soil natural regime and multiple cropping system applied. In addition, flooding often has obvious temporal and spatial variations, as it is influenced by local topographic and weather conditions; thus, the influence of flooding variations is always localized [30]. Thus, given the complex agricultural conditions in the MLYRB and the localized impact of flooding, it is difficult to derive the localized influence of flooding on crop production over such a large basin.

Satellite remote sensing seems to be a feasible tool in terms of obtaining spatially explicit maps of the localized impacts of (or damage caused by) flooding over large-scale areas with a sufficiently high spatial resolution. Some studies have attempted to use the difference in crop growth condition between pre-flood and post-flood periods [31–33] or between the flood years and normal years of post-flood periods [34] from remote sensing imagery for this purpose. Our previous study [35] uses the difference of vegetation index between the flood year and harvest year to obtain the crop yield losses caused by flood disaster. However, these extreme flood events in the Yangtze River are characterized by a long duration (often more than a month). Over such long periods, crop systems may naturally grow or die. The intra-annual and inter-annual variations in crop systems’ vegetation greenness are relatively large even without external disturbances [36,37]. Obviously, the differences in crop growth conditions between pre-flood and post-flood periods or between flood years and normal years will be affected by both flood disturbances and natural variations, meaning that this method cannot be applied to the MLYRB. In another previous study [38], the comparison of maximum crop greenness between the years with and without flood disturbances was used in order to quantify the influence of flooding on crop growth, avoiding including the effect of crop natural growth during the growing period. Yet, the comparison of maximum greenness only applies to single-cropping systems and flood events occurring before crops reach maximum greenness. Thereby, a new satellite-based index is developed in this study to identify the spatially explicit influence of flooding on crop production for long-duration floods and multi-cropping agricultural systems.

Besides the consequences of flooding, the importance of the comprehensive evaluation of flood risk has been increasingly taken into account by combining data on hazard and vulnerability of flood-affected areas [39,40]. At present, comprehensive evaluations of flood risk are largely implemented through laboratory testing or model evaluation. Waterlogging testing under controlled depth and duration offers basic information on the biophysical response of crops to submersion [41–44]. However, such experimental findings have limited value in extrapolation to the real world due to the extent of differences between places. To avoid the limitations associated with laboratory testing, a variety of mathematical models have been developed to examine the relationships between crop yield losses and flood events. Mathematical models of this type mainly fall into two categories—i.e., statistical [30,45] and mechanistic [46]. Statistical models relate crop yield fluctuation to various flood or meteorological variables by regression or other more sophisticated statistical methods. This type of statistical estimation can be used to quantify the effects of flooding on agricultural production from a broad-scale perspective—e.g., the national or province/state scale. However, these statistical methods are incapable of considering the influence of localized flooding variations. Mechanistic models utilize the biophysical principles of crop, soil, weather, and management interactions to predict the crop yield [47]. Due to the high data demand for the determination of parameters associated with crops, soil, and

management in mathematical terms, the data are often sparse; consequently, these mechanistic models cannot be applied to large-scale area. Thus, in order to comprehensively evaluate agricultural flood risk, spatially explicit, temporally dynamic, and sufficiently high-spatial-resolution maps of flood characteristics are needed.

Recently developed 2D hydraulic models offer the possibility of obtaining spatial and temporal field information of flood evolution. Water flows are described in terms of continuity and momentum principles and discretized over a grid of cells, which allows the models to depict 2D dynamic flow fields based on the topography of the riverbed and floodplain [48]. Thus, 2D hydraulic models can provide spatially explicit and temporally dynamic pictures of flood characteristics for the whole computational domain. While some existing 2D hydraulic models are capable of capturing inundation fields, often they only show a very small basin [49–53] or a single river reach [48,54], or have a coarse resolution [55] due to the high computational expense involved. One practicable approach proposed to improve the computation speed of 2D hydraulic models is model parallel computation with a graphics processing unit (GPU), which can provide catchment-scale 2D flood simulations at high resolutions involving millions of computational cells. Some studies have made exploratory attempts and achieved feasible results [56–60]. Thus, the accessibility of high-performance computing could make it possible to derive a spatially explicit and temporally dynamic map of flood characteristics over a large-scale watershed, ensuring the consistency of spatial resolution between flood damage evaluations based on remote sensing imagery and 2D flood simulation. Additionally, it is possible to investigate the highly localized impacts of flooding on crops—i.e., the flooding of individual fields—and implement a comprehensive evaluation of the agricultural flood risk.

Therefore, this study aimed to comprehensively evaluate the agricultural flood risk, focusing on the combination of flood hazard and the consequences of flooding on crops, considering the characteristics of flooding impacts with a strong spatial and temporal variability. Specifically, three problems were solved: (a) what the spatial–temporal characteristics are of the consequences of flooding on crop growth; (b) what the features are of flood inundation patterns and evolution processes; (c) what the relationship is between flood characteristics and crop damage from flooding. The investigation framework consisted of the following three parts: (a) an integrated disturbance index (IDI) based on remote sensing imagery was developed in this study to identify the flood impact on crops from the backdrop of natural fluctuations in the crop systems for long-duration floods and multi-cropping agricultural systems, aiming to acquire spatially explicit and sufficiently high spatial resolution maps of the crop damage condition over large-scale areas; (b) a 2D hydraulic model parallelized using the GPU approach was employed to simulate the flood dynamics, aiming to derive enough meaningful details at the local scale in terms of flood inundation patterns and processes over the whole natural watershed; (c) the random forest model was used to relate the crop yield loss and flood characteristics, aiming to investigate the relationship between flood hazard and consequent damage. The proposed evaluation framework will be tested in the MLYRB, where the severe flood event in 2010 caused great agricultural losses during the crop growing season.

2. Materials and Methods

2.1. Conceptual Model for Monitoring Flood Impacts on Crop Growth

Excessive rainfall and associated waterlogging can seriously impede plant growth and lead to significant yield losses in many crop species. Flash floods may wash away or ruin entire swaths of agricultural land and completely destroy crops. Besides the direct damage caused by flooding, waterlogging resulting from heavy rainfall with a long duration also adversely affects crop production, mainly through restricting gaseous exchange in the soil [61]. Consequently, crop yield subjected to soil submergence can decrease significantly [62,63]. At the same time, previous experiments have suggested that crops exposed to waterlogging have the capacity to recover after stress is released [64–66]. Thus, the final flooding damage caused to crops depends not only on the stress conditions but also on

the subsequent recovery status after stress is released. The Moderate Resolution Imaging Spectroradiometer (MODIS) with its high-frequency sampling (twice daily) provides a valid tool for tracking the temporal trajectories of crop growth dynamics. The vegetation indices (VI) from MODIS are commonly used to statistically correlate to crop growth conditions and yield across the world [67,68]. The trajectory of vegetation indices can help us to detect flooding disturbance and characterize the subsequent recovery of crops, thus making it ideal for identifying the final impact of flooding on crop production.

Previous efforts have shown the potential of VI temporal trajectory analysis in generating parameters for crop yield estimation, such as the integrated greenness and peak greenness. The integrated greenness—i.e., summing the VI values at regular intervals during the crop growing season—can be used to roughly represent the accumulation of green leaf area. It has been shown to be an excellent measure of the produced biomass and crop yield [38,67,69–71]. Given that the crop growth dynamics during the full time period can be considered in the integrated VI, it is more ideal than individual VI observations for long-duration flood events. Additionally, the use of integrated VI helps us to distinguish the effects of the growing season of flood-affected crops in a multi-crop agricultural system. Better yet, integrated VI can combine the effects of both the flooding disturbance (indicated by the red area in Figure 1) and the possible recovery (indicated by the green area in Figure 1). Thus, the integrated VI is adopted in this study.

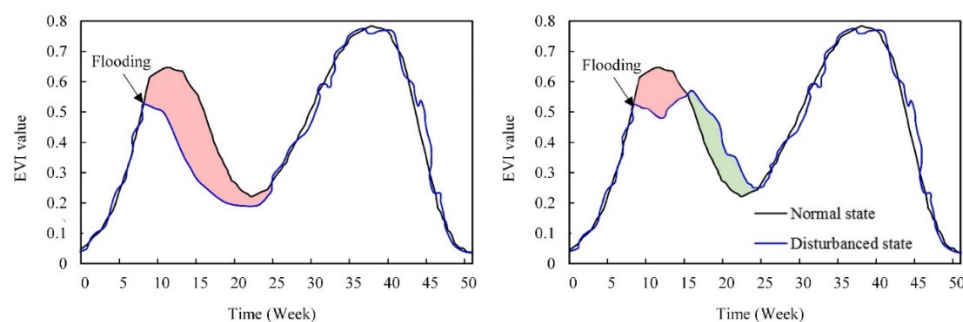


Figure 1. The conceptual model illustrating the effect of flood disturbance on crop production. The red area represents the effect of the disturbance of flood on crop growth, and the green area represents the subsequent recovery of the crop.

Recently, different types of VIs have been proposed. The Normalized Difference Vegetation Index (NDVI) and the Enhanced Vegetation Index (EVI) are the most extensively used indices for the statistical analysis of crop growth conditions [72]. The newly released EVI has been shown to have greater potential in monitoring crop yield than NDVI [73,74], owing to the fact that EVI remains sensitive in dense vegetation while NDVI is saturated [75,76]. Therefore, EVI and integrated EVI (IEVI) are adopted in this study and may be calculated by the following formula:

$$EVI = 2.5 \times (R_{Nir} - R_{Red}) / (R_{Nir} + 6 \times R_{Red} - 7.5 \times R_{Blue} + 1) \quad (1)$$

where R_{Nir} , R_{Red} , and R_{Blue} refer to the reflectance of the near-infrared, red, and blue bands of remote sensing images, respectively.

$$IEVI = \sum EVI_t \quad (2)$$

where t represents the time period of the crop growing season and EVI_t is the EVI value in time period t .

Flood impact on crop production can be seen as one type of terrestrial disturbance that occurs outside the range of natural variations [77]. In the absence of disturbances, crops are expected to reach their maximum greenness for a specific environment, and natural fluctuations in hydrothermal balance manifest physiologically as interannual variability

in crops' EVI value. The magnitude of the interannual fluctuations is usually large in agricultural ecosystems. Therefore, a fine-tuning of change thresholds is necessary in order to separate true disturbances from natural fluctuations. The integrated disturbance index (IDI) is defined as follows:

$$IDI = 1 - IEVI/IEVI_{max} \quad (3)$$

where IEVI is the integrated EVI value of the current year and $IEVI_{max}$ is the multi-year mean of IEVI without external disturbances. In this study, the analysis is based on the number of years (17 years) of available data, and the top 50% of the IEVI is used in the calculation to derive the crop's IEVI without external disturbances. As for the range of natural fluctuations, we use one standard deviation (SD) from the mean IEVI without external disturbances for each individual pixel as the disturbance threshold. Pixels that fall within ± 1 SD of the multi-year mean are considered to be within the natural fluctuations for that individual pixel. Pixels that depart significantly (beyond 1 standard deviation) from the long-term mean IEVI are identified as areas of potential disturbance. When a flash flood occurs, the IDI in the damaged area will decrease to a certain level that is obviously less than the multi-year mean. The negative impact from this flood event (as shown in Figure 1 left) will be detected when it shifts outside the range of natural variations. As the damaged area recovers after stress is released, the IDI should fall inside the range of natural fluctuations (as shown in Figure 1 right). Although simple, the IDI is thus ideal for identifying the final impact of flooding on crop production.

2.2. Coupled Hydrological and 2D Hydraulic Model for Flooding Simulation

The coupled model uses the SCS-CN hydrological model as a rainfall-runoff generator and implements the routing scheme with the 2D hydraulic model in order to simulate localized flood depths, durations, and velocities. The Soil Conservation Service-Curve Number (SCS-CN) model [78] is an event-based model that estimates hydrologic losses and transforms rainfall to runoff with a rainfall-runoff curve. The curve varies according to a parameter called the curve number (CN). The dimensionless CN represents the antecedent potential water retention of a watershed [79]. The SCS-CN model has been widely used all around the world over various hydro-meteorological conditions because the CN value can be tabulated considering hydrologic conditions, land use types, and soil types. Detailed information on it can be found in the study of Mishra and Singh [80]. In this study, the surface runoff is computed with the SCS-CN for every cell in every time step in order to be consistent with the spatio-temporal resolution of the 2D hydraulic model. The calculation procedure used can be found in Caviedes-Voullième et al. [49].

For the hydrodynamic component, surface flow is simulated by means of the depth-averaged 2D shallow water equations. Floodplain flow modeling using shallow water equations has been extensively explored [81–86]. Shallow water equations can be thought of as a simplification of the Navier–Stokes equations, assuming the pressure distribution to be hydrostatic—i.e., neglecting the vertical acceleration term [87]. In shallow water models, the horizontal wavelength is much larger than the vertical dimension and the streamlines remain approximately parallel to each other [88]. The conservative matrix form of the 2D shallow water models may be expressed as follows:

$$\frac{\partial \mathbf{q}}{\partial t} + \frac{\partial \mathbf{f}}{\partial x} + \frac{\partial \mathbf{g}}{\partial y} = \mathbf{s} \quad (4)$$

where t is the time; x and y are the Cartesian coordinates; \mathbf{q} is the flow-variable vector; \mathbf{f} and \mathbf{g} denote the flux vectors in the x and y direction, respectively; and \mathbf{s} is the source term vector.

$$\begin{aligned}
 \mathbf{q} &= \begin{bmatrix} h \\ q_x \\ q_y \end{bmatrix} & \mathbf{f} &= \begin{bmatrix} q_x \\ uq_x + \frac{1}{2}gh^2 \\ uq_y \end{bmatrix} \\
 \mathbf{g} &= \begin{bmatrix} q_y \\ vq_x \\ vq_y + \frac{1}{2}gh^2 \end{bmatrix} & \mathbf{s} &= \begin{bmatrix} R \\ -C_f u \sqrt{u^2 + v^2} - gh \frac{\partial z_b}{\partial x} \\ -C_f v \sqrt{u^2 + v^2} - gh \frac{\partial z_b}{\partial x} \end{bmatrix}
 \end{aligned} \tag{5}$$

where h denotes the water depth (m); q_x and q_y denote the unit-width discharges in the x and y directions (m^2/s), respectively; u and v are the depth-averaged velocities in the x and y directions (m/s), respectively; $q_x = uh$ and $q_y = vh$; R is the generated runoff rate from the SCS-CN model (m/s); z_b is the bed elevation (m); and C_f is the bed roughness coefficient ($\text{s m}^{-1/3}$).

The shallow water equations are solved by means of a first-order Godunov-type finite volume scheme. Finite volume schemes allow simulations of flood propagation to be carried out on real irregular topography, and its predictions are robust and accurate [57,89]. However, it is widely known that finite volume schemes heavily rely on mesh size and have a high computational cost as the number of cells within the domain increases [49]. The increased computational time can become a crucial issue, since the complex topography of large-scale catchments leads to a very large number of cells. To overcome this issue, this study carries out flood simulations on Graphics Processing Units (GPUs) using NVIDIA's parallel computing architecture CUDA (compute unified device architecture) [90], thus taking advantage of the parallel numerical schemes of modern graphics cards.

The topography of channels and floodplain is another of the most important factors determining the performance of 2D hydraulic models. However, the currently available global topographic data have limitations regarding their application in flood modeling, mainly due to their random errors and insufficient spatial resolution [91]. To ensure the modeling accuracy of the 2D hydraulic model, we apply a newly released DEM (i.e., Multi-Error Removed DEM) which corrects major error components in the Shuttle Radar Topographic Mission DEM (SRTM DEM) [92]. Additionally, a hydraulic correction method [93] is employed for the MERIT DEM to improve the flow connectivity of river networks, which can reduce the limitation of insufficient spatial resolution to some extent. Then, the hydraulically corrected DEM is used to enhance the flood inundation modeling.

2.3. Random Forest Model for Identifying Flood Impact on Crop Production

In the MODIS-based crop yield losses and 2D hydraulic flooding simulation results, it is essential to identify the relationship between crop response and predictors and then recognize the most important influence variables of floods that impact crop production. As a machine learning method, random forest has a good tolerance to outliers and noise, and strong robustness, which leads to a wide range of application prospects [94]. Random forest provides two kinds of importance measures: Mean Decrease Impurity (MDI) based on the Gini index and Mean Decrease Accuracy (MDA) based on Out-of-Bag (OOB) data [95]. In this study, the random forest model is used to relate the crop yield losses to flood characteristics. Random forest models create a "forest" out of an ensemble of decision trees. Each tree is created using a sample of two-thirds of the data and a randomly permuted subset of the explanatory variables. One-third of the data are left out and used to test the performance of that tree. For each explanatory variable, the importance metric can be determined by the difference in performance between decision trees with and without a given variable permuted. Using a random forest model, the functional forms relating response and predictors can be displayed using partial dependence plots [96]. In this study, a random forest model was created using the "Random Forest" package [97] in R [98].

2.4. The Study Area and Events

The middle and lower reaches of the Yangtze River Basin (MLYRB) are located at 24 to 35° N and 109 to 122° E, mainly including the provinces of Hubei, Hunan, Jiangsu, Zhejiang, Anhui, and Jiangxi and Shanghai municipality (Figure 2). The annual average temperature ranges from 14 to 18 °C, and the annual mean rainfall is approximately 1000–1400 mm [99]. The basin is characterized by a cold-dry winter and warm-wet summer, and 70–80% of its rainfall occurs in the summer [14]. Appropriate climate conditions make this region one of the most important agricultural areas in the world. It accounts for 24.5% of China's crop-harvesting area and accounts for nearly 28.6% of the grain production in China. However, due to the fact that the Yangtze River is almost parallel to the subtropical monsoon rain belt (i.e., Meiyu front), the agricultural production is vulnerable to floods and always afflicted by crop failure from waterlogging.

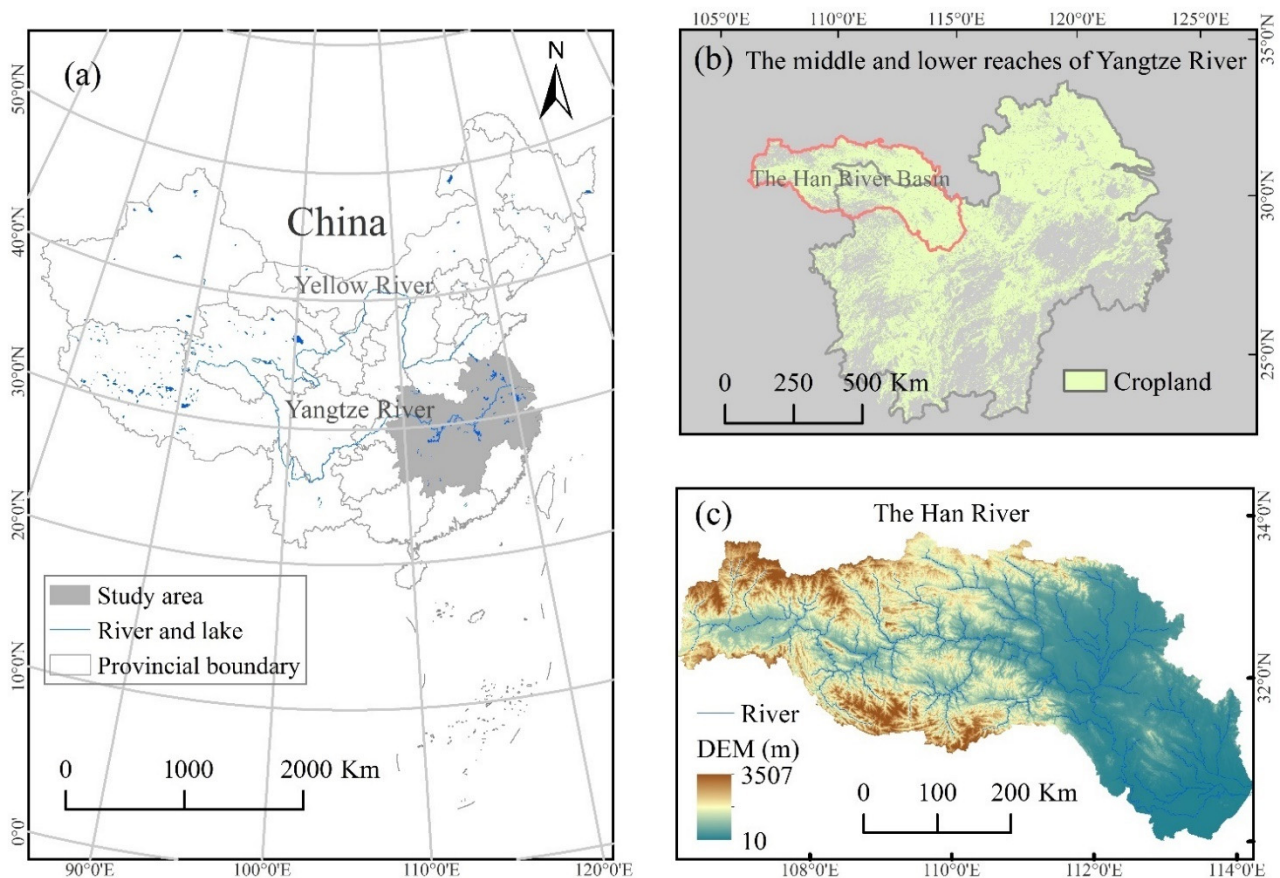


Figure 2. The study area: (a) China; (b) the middle and lower reaches of Yangtze River; (c) the Han River.

From June to August in 2010, an extreme flood event with a record high water discharge hit the Yangtze River, causing immense economic losses and casualties (see http://en.wikipedia.org/wiki/2010_China_floods, accessed on 24 January 2022). According to GRACE data analysis, the discharge and precipitation of this rainstorm disaster were 38% and 19% higher than the average for previous years [100]. Additionally, this flood was characterized by a long flood duration and wide influence scope; thus, it has been identified as the most serious flood disaster since 2000. According to annual report on natural disasters in China, approximately 100 million people were affected; 2027 people were killed, 620 thousand houses were damaged, 52 thousand square kilometers of land were affected, and the economic losses may have been as high as 125 billion yuan [101].

A flood inundation simulation utilizing the coupled hydrological–hydraulic model was implemented in the Han River, the largest tributary of the MLYRB, and then used to

identify how flood characteristics affect crop failure (Figure 2). The Han River is located at $30^{\circ}10'–34^{\circ}20' N$ and $106^{\circ}15'–114^{\circ}20' E$, with a $159,000 \text{ km}^2$ basin area. The basin is situated in the humid zone with a sub-tropic monsoon climatic environment. The annual average temperature ranges from 12 to $16^{\circ} C$. The annual average precipitation is $700–1800 \text{ mm}$, with high intra-annual and inter-annual variations [102], and 80% of the precipitation is concentrated during the period from May to October [103]. These extreme rainstorms occurring in the early summer and the long periods of rainfall often lead to flooding and waterlogging disasters occurring in the Han River Basin.

2.5. Data Acquisition

The MODIS EVI dataset for the period from 2000 to 2016 were provided by the NASA Earth Observing System (EOS). Although MODIS sensors provide nearly complete Earth coverage every day, the daily measurements are frequently contaminated by clouds, aerosols, and cloud shadows [104]. The cloud contamination is more serious during flooding events [105]. To help reduce the effects of cloud interference, the MOD13Q1 version 6 product was retrieved, which provides the 16-day EVI at a 250 m resolution. The 16-day dataset is a maximum value composite (MVC), in which the pixel observation with the highest EVI value is adopted to represent the compositing period (16 days). MVC selects the least contaminated observations and tends to adopt the closest near-nadir view [106]. Moreover, all unreliable pixels are removed according to the MOD13Q1 reliability layer (value) before the EVI data are adopted.

The HJ-1A/B satellites are China's two small environment satellites; they were launched on 6 September 2008. The CCD images of the HJ-1A/B satellites with a 30 m resolution, which were acquired during the 2010 flood event, were derived from the China Centre for Resources Satellite Data and Application and used to map the water surface area and validate the flood simulation result. The hourly precipitation dataset was provided by the National Climate Center (NCC) of the China Meteorological Administration (CMA). This dataset was constructed based on a 0.1° attitude-longitude grid covering the period from 2008 to now by merging two kinds of information sources with different characteristics, including more than 30 thousand automatic meteorological stations and the CMORPH satellite-based global rainfall product. Land use data were obtained from the GlobCover 2009 dataset, which was created based on 300 m Medium-spectral Resolution Imaging Spectrometer (MERIS) data by the European Space Agency (ESA) and Université Catholique de Louvain (UCL) [107]. Soil type information was provided by the harmonized world soil database [108]. Additionally, this study adopted the "Multi-Error-Removed Improved-Terrain DEM" (MERIT DEM) with a spatial resolution of 90 m [92]. River networks with a 15 arc-second resolution were derived from the HydroSHEDS datasets [109]. In order to maintain consistency with the spatial resolution of the MODIS EVI product, the precipitation data, land use data, and DEM were all resampled to a pixel size of $250 \text{ m} \times 250 \text{ m}$ using the nearest neighbor algorithm. In addition, the flood-affected crop areas for the 2010 flood event were collected from information provided by the Ministry of Agriculture. When more than 10% of the expected crop yield of the cultivated land was reduced by flooding, the affected areas were counted in the agricultural disaster statistics [110].

2.6. Study Framework

As shown in Figure 3, this study comprises three main steps:

- (1) The calculation of integrated disturbance index (IDI). The integrated disturbance index (IDI) was applied to the MODIS EVI dataset for 17 years.
- (2) Flood Simulation. The spatial surface characteristics and precipitation were input into the coupled SCS-CN and 2D hydraulic model, and the flood process was simulated for MLYRB with GPU parallel computing.
- (3) The integrated impacts of flood on crop yield loss. Random forest was adopted to predict the crop damage extent with different flood characteristics.

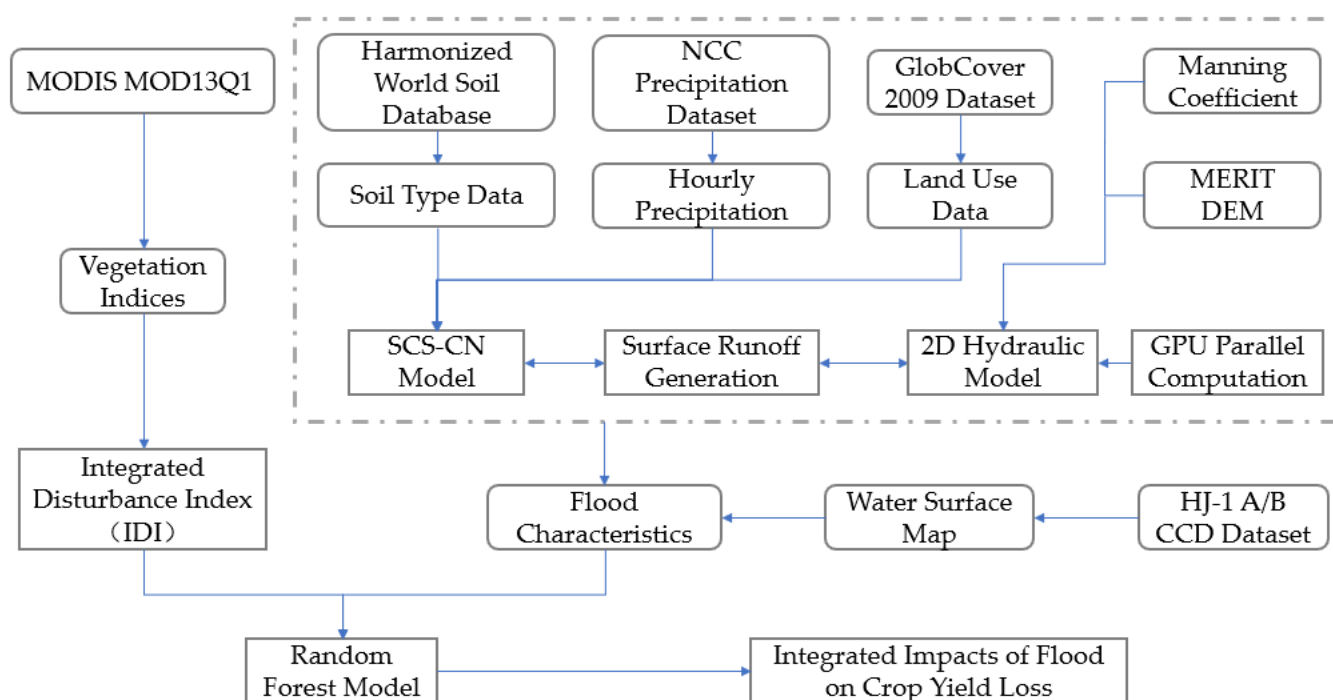


Figure 3. The study framework.

3. Results

3.1. The Characteristics of Flood Disturbances on Crop Yields

The integrated disturbance index (IDI) proposed in this study was applied to the MODIS MOD13Q1 data for the years 2000–2016 across the MLYRB. In the study area, two or three harvests a year are grown instead of one. In order to investigate the influence of flooding on the current crop, the IDI value was based on the EVI of crops after flooding. The 2010 flood event mainly took place in the MLYRB from late June to July. We analyzed the MODIS EVI from late June to early September, including day 209, day 225, and day 241 of the 16-day composites. Figure 4a displays the IDI values across the croplands of the MLYRB. Given that the Ministry of Agriculture defines a 10% loss of crop yield as the threshold recorded in the national disaster dataset, an IDI of more than 10% and beyond one standard deviation was determined as the criterion for flagging a pixel as disturbed. Based on this criterion, 85,887 km² of croplands across the MLYRB were determined to be impacted by external disturbance. The statistics released by the government showed a flood-affected area of 81,404 km² in the MLYRB. The satellite-based detection result was very close to that shown by the statistical data, and the error between them was only 5.5%. According to the governmental reports and related news reports, the main streams of the Yangtze River (including Jianli, Luoshan, Hankou, Jiujiang, and Datong), Dongting Lake Basin, Poyang Lake Basin, and Han River Basin were the areas that were most heavily damaged during the 2010 flood event. Additionally, the Fu River, Xin River, and Gan River within the Poyang Lake Basin were the most hard-hit areas, with the discharge reaching a 50-year return period. The main river in the Dongting Lake Basin, the Xiang River, was also seriously damaged, with the water level reaching the third largest level recorded. Some tributaries of the upper reaches of the Han River were also among the most hard-hit areas. From Figure 4a, it can be seen that most of the cropland pixels that were obviously disturbed by flooding (shown in red) were basically distributed around Dongting Lake and Poyang Lake and along the main stream of the Yangtze River. The satellite-based detection results were, on the whole, consistent with the most hard-hit areas recorded (shown in blue in Figure 4a).

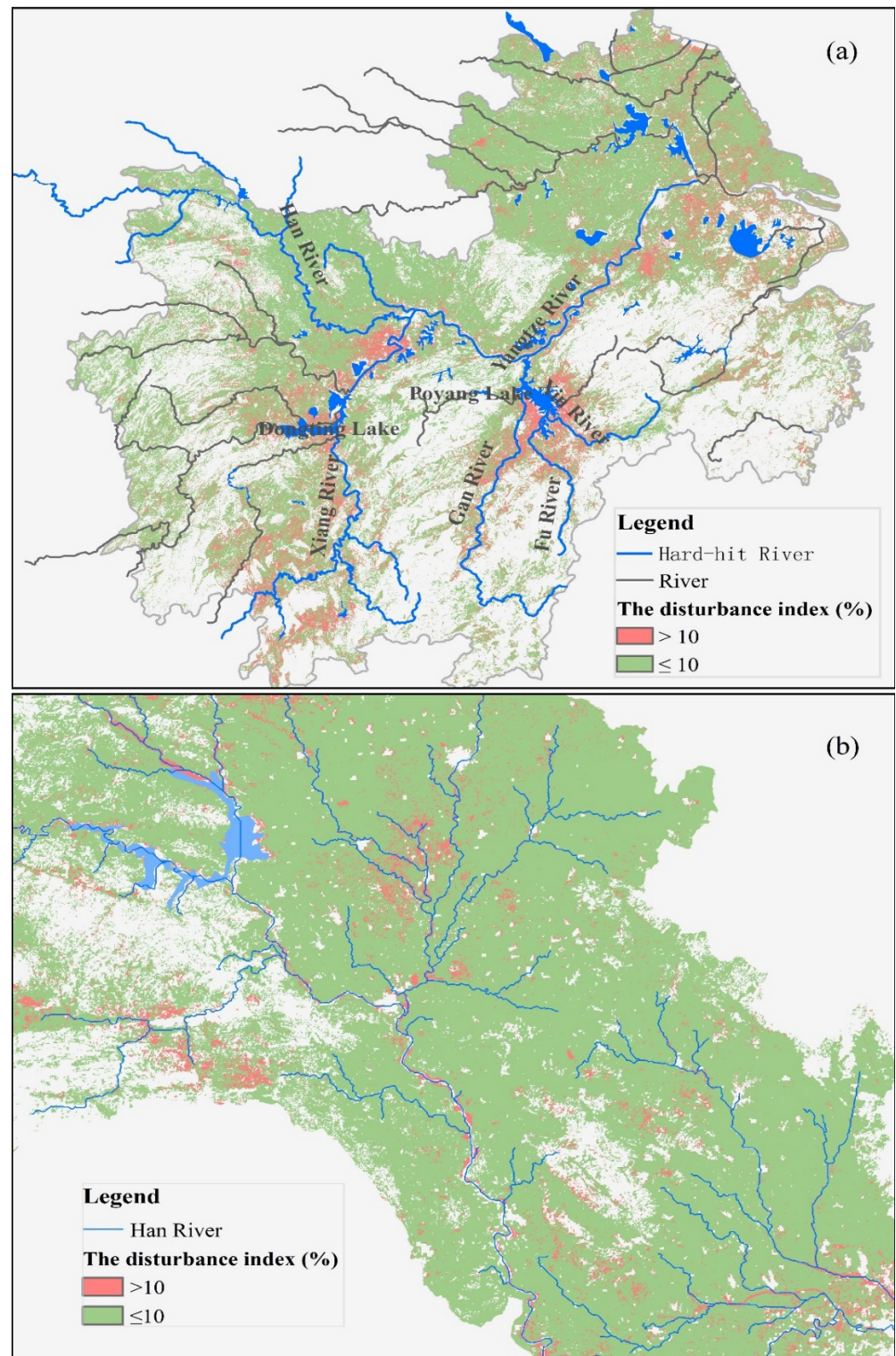


Figure 4. Flood disturbance detection results obtained from the IDI in (a) the middle and lower reaches of the Yangtze River Basin (MLYRB) and (b) the Han River Basin.

In addition to validating the detection results obtained throughout the whole study, their accuracy was also verified with spatially compatible field data. Given the difficulty of deriving field investigation data over large areas through postsurveys, the spatial characteristics of the obviously disturbed croplands were investigated based on the physical characteristics of the river floods. In addition to areas where surface water concentrates, the

interaction between rivers and floodplains is crucial in the evolution of flood events. Often, flood inundation emanates from overflow river systems and expands into the surrounding areas. Tehrany et al. [111] showed that flooding mainly occurs near to the riverbank and that a distance from the drainage network of within 1700 m is positively correlated with flood occurrence in flat areas. Kazakis et al. [112] also indicated that areas near a drainage network are highly vulnerable to flood hazards, and that flood hazards decrease at distances from the drainage network >2000 m by analyzing records of historical floods that occurred in the Rhodope-Evros region, Greece. Other similar results can be found in Samela et al. [113] and Tang et al. [114]. Distance from streams usually has a major influence on the velocity and extent of flooding in flat areas. From Figure 4b, in the Han River Basin, it can be seen that most of the pixels that are obviously disturbed by flooding (in red) are distributed near to streams. In order to quantitatively and objectively evaluate our results, the distance between disturbed pixels and the nearest rivers was calculated in ArcGIS, and the analysis domain does not include these concentrated disturbed areas (around Doting Lake, Poyang Lake, and the main stream of the Yangtze River). The results are shown in Table 1 as 47% and 74% of the disturbed pixels are, respectively, within 1000 m and 2000 m from river streams. This indicates that most of these disturbed pixels are concentrated in the riparian zones. The spatial characteristics of flood-affected crop areas were in agreement with the potential flood-prone areas, as expected. This indirectly verifies the spatial characteristics of the detected flood-disturbed areas as well as the validity of the satellite-based IDI proposed in this study for flood impact detection.

Table 1. Percentage of the flood-disturbed areas within a certain distance to the nearest stream.

Distance (km)	<0.1	[0.1, 0.2)	[0.2, 0.5)	[0.5, 1.0)	[1.0, 1.5)	[1.5, 2.0)	[1.5, 2.0)
Percentage	7	13	28	47	62	74	83

Traditionally, flood impact detection is implemented by combining the identified agricultural lands affected by inundations and “loss functions”. Firstly, inundation maps are derived by different approaches, including DEM analysis [115], the interpretation of remote sensing imagery [116], and hydrodynamic simulation [117–121]. Then, the agricultural lands affected by flooding are identified by overlying the inundation maps with land use maps. Lastly, “loss functions”, which describe the relationship between flood intensity (e.g., water depth) and associated damage, are used to estimate the crop damage caused to affected areas. However, it is hard to derive the loss functions suitable for specific study areas, which are regarded as the key factors in traditional methods, because historical flood damage data are generally scarce and unlikely to be available [120]. In this study, we make use of the information of MODIS imagery with high frequent sampling and a relatively long data archive, which can be used to track the temporal trajectory of the vegetation index during the crop growing season. An effective and scalable index was designed to detect the flood disturbance signal from the natural variation signal for the complicated multi-cropping agricultural systems. Relative to previous methods, this evaluation index had the advantages of a higher efficiency and lower computation burden. It had the capacity to quantify the actual flooding damage, taking into consideration the direct influence of the flood and the subsequent crop recovery status. Moreover, this index is relatively simple and mainly based on globally accessible data; it does not necessarily require the division of crop growing seasons and is especially useful for complex agricultural systems that follow multi-cropping practices.

3.2. Flood Simulation Results

The coupled hydrological and hydraulic model developed in this study was implemented to predict time-varying and grid-based flood depths, velocities, and durations within the whole Han River Basin for the July 2010 event. The spatial resolution of the

2D hydraulic model is 250 m. The calculating duration is the same as the precipitation duration, and the length of dynamic calculating step is about 1 s.

Figure 5 highlights the spatial distribution of the maximum water depth, flow velocity, and flood duration for each pixel. The strength of the coupled model is exemplified by this series of maps, as they offer a clear picture in terms of the flood process and pattern while simultaneously ensuring a sufficiently high spatial resolution, which makes it possible to investigate the highly localized impacts of flooding on individual crop fields.

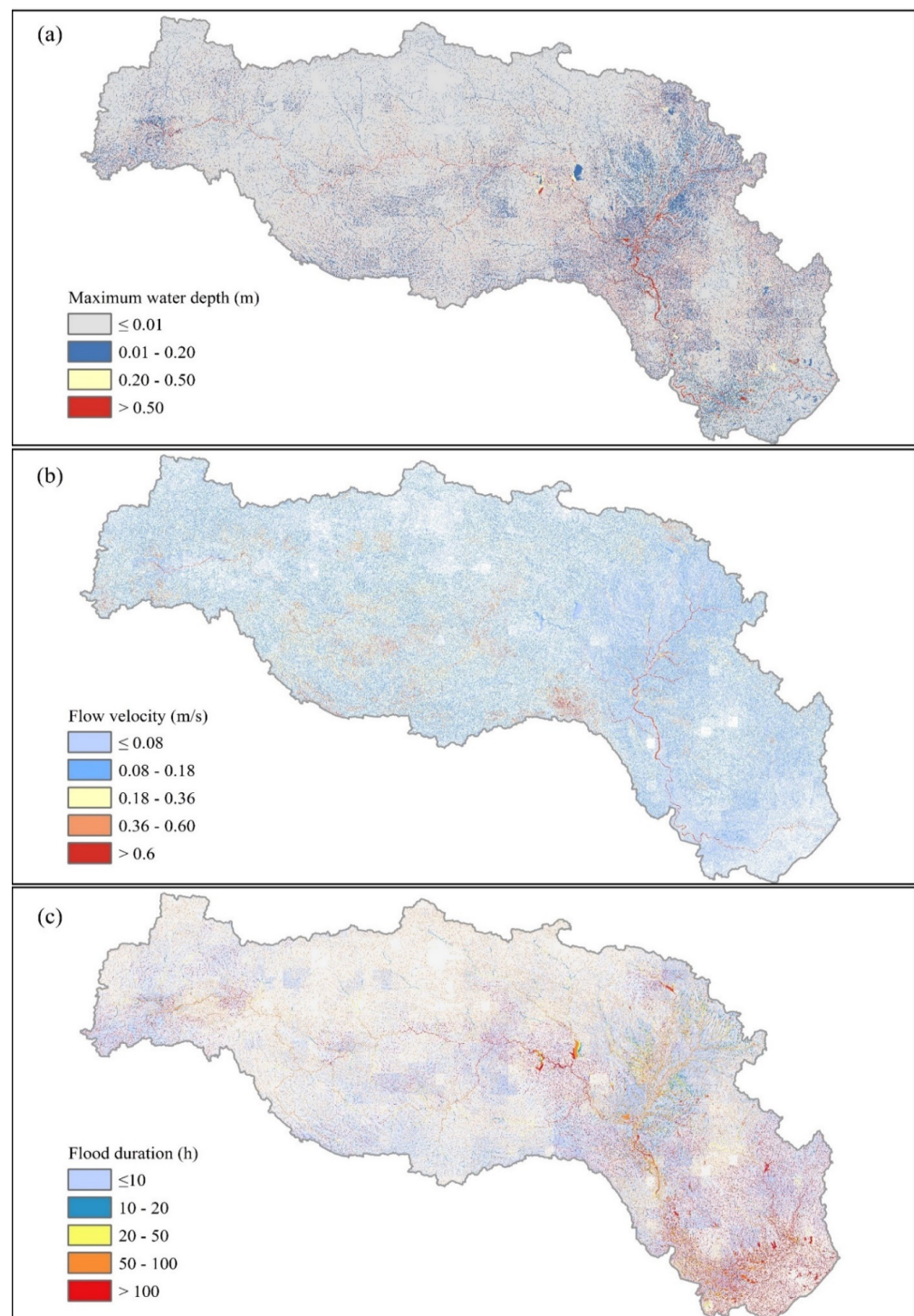


Figure 5. Flood simulation results of (a) maximum water depth, (b) flow velocity and (c) flood duration for the Han River Basin.

According to the simulation results, the total precipitation was 117.5 mm for the entire storm, which resulted in a mean maximum water depth of 80.3 mm (as shown in Figure 5a). The predicted maximum water depth spatially varied from 0 mm to 30.3 m during this flood. Therefore, the percentage of water with a depth of more than 0.01 m and 0.1 m was 20.1% and 9.6%, respectively. Besides flooding depth, the coupled model provided a refined description of flow velocity, highly influenced by the topography. The velocity of flow in the floodplain was found to vary between 0 and 1.5 m/s (as shown in Figure 5b). Moreover, the proposed model could also be used to predict the flood duration (as shown in Figure 5c).

The evaluation of the flood inundation simulations was implemented using HJ-1A/B CCD images of the event acquired from 21 July to 3 August. The surface water area was extracted from these images using a supervised classification model. The surface water area, including rivers, lakes, and pond areas, can be most easily identified when image pixels are not impacted by cloud cover. Based on previous research on this topic [122–124], extracting water body information from HJ-1 A/B CCD datasets is an effective method, and the overall accuracy can reach as high as 93.82% [122].

The simulated maximum water depth of 2D hydraulic model and the surface water areas extracted from HJ-1 A/B CCD images were overlapped, and the intersecting part was analyzed across the Han River Basin. In Figure 6, the intersection of the water body area of HJ-1 A/B CCD (as the observed results) and the simulated results is shown in different colors for different depths. As the extent of the surface water areas is significantly lower than that of the actual flood footprint because overland runoff can flow past certain areas without forming open water (i.e., boundaries of inundated areas) [125], we defined those areas where the simulated maximum water depth was above 20 mm as the predicted correct areas. As Figure 6 shows, the predicted correct area accounted for 87.6% of the intersection area, which means that the accuracy of the validation was 87.6%. Therefore, the percentage of predicted water depth of above 50 mm and 100 mm in the surface water area was 76.3% and 50.7%, respectively. This result shows a favorable agreement between the numerical modeling and remote sensing data for the coupled hydrological and 2D hydraulic model.

This study may contain biases for neglecting the control facilities. For example, in the case of continuous levees, the lowest point of the levee height overflows or breaks the levee. The artificial levee would raise the flood risk by decreasing the water storage capacity of river, which leads to flood water either overtopping the bank or breaking the levee and creating the flood during heavy rain [126]. The flood inundation area, water depth and flood duration could be reduced by storing the flood water in the reservoir behind the dam during flooding time. A case study in Bago River Basin, Myanmar, shows that the dam operation for flood control would reduce the flood inundation area by approximately 10% and crop field damage by approximately 10% [127]. However, based on the overlapped images of simulated water depth of hydraulic model and water body area from HJ-1A/B CCD images, the validation of the flood simulation, in the hypothesis that the area where the simulation water depth was less than 20 mm would be excluded, are reliable.

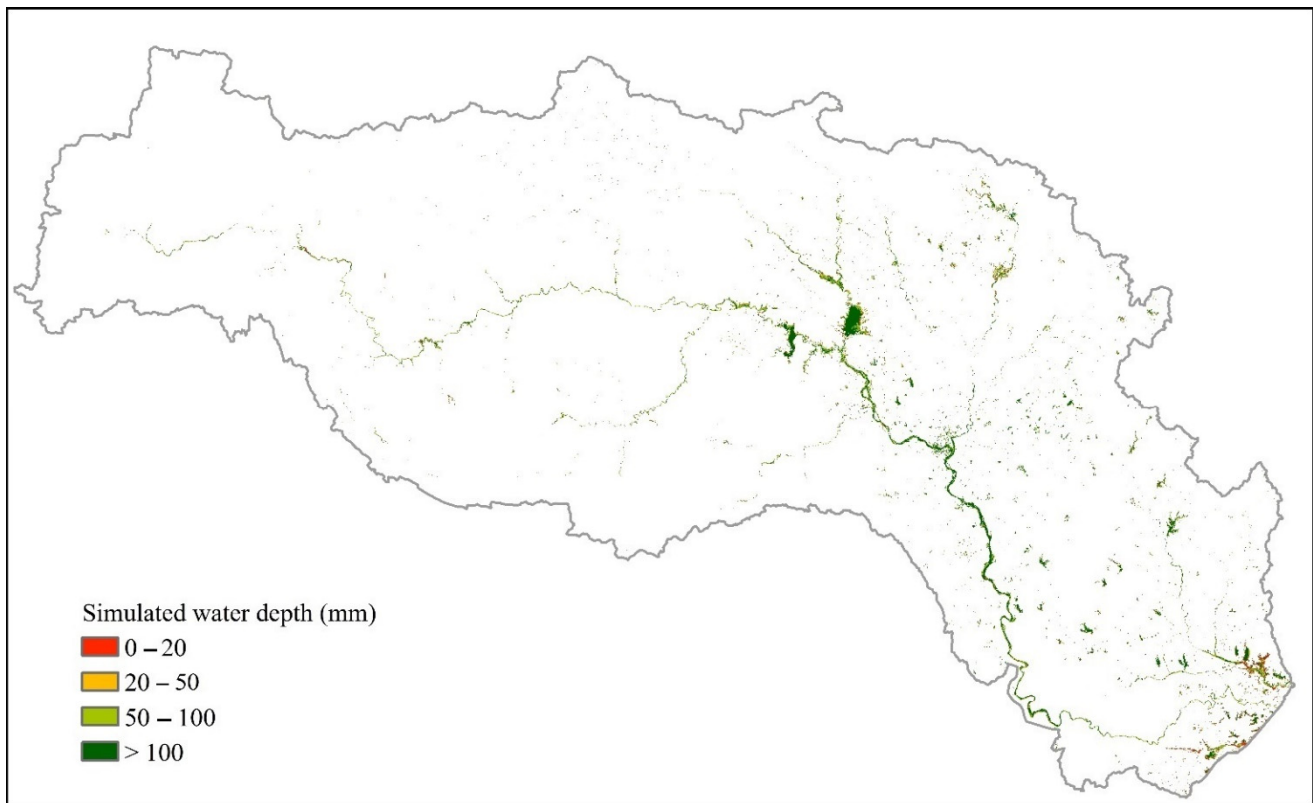


Figure 6. Comparing the modeled water surface area with HJ imagery.

3.3. The Relationship between Flood Characteristic and Crop Damage Extent

After accomplishing the detection of flood disturbance of crops based on the IDI index from the MODIS EVI dataset and flood inundation simulation via coupled hydrological–hydraulic model, the crop damage extent and flood characteristics could be derived for each pixel over the whole basin. Subsequently, the average values of each flood variable (including the maximum water depth, mean water depth, flow velocity, and duration) for pixels with the same crop damage extent, and thereby the distribution of flood variables against every 1‰ crop damage extent, could be acquired. We then adopted random forest analyses to predict the crop damage extent with these flood characteristic predictors. The variable importance calculation ranked the importance of flow duration (h), flow velocity (m/s), maximum water depth (m), and mean water depth (m) for the integrated disturbance index (IDI). The *n*tree was set to 500, and the width and height of the tree were set to 14 and 8, respectively. Additionally, relationship between crop yield losses and each variable is plotted in Figure 7.

The results from the random forest analysis suggest that the flood duration and flow velocity are positively correlated with the crop damage extent, as expected. However, the water depths, including maximum and mean depths, did not show obvious correlation with the crop damage extent. The flood duration was the most important predictor in our analysis. Although in previous evaluations of flood damage to agricultural production, water depth is most commonly used and is considered to be the most influential flood parameters [128]. Compared to previous research by Vempi and Komori in 2021 [129], the most important flood parameter of the maximum water depth, maximum flood duration, and maximum flow velocity to crop yield loss is the maximum water depth. The relationship between flood characteristics and crop yield losses varies for different physical condition of the study area. Yet, the Han River Basin shows different features mainly due to its own watershed characteristics. The Han River is characterized by a high level of precipitation and siltation, but unfavorable water discharge. Due to siltation, the riverbed has kept rising over the last nearly 400 years; consequently, there is a difference of several

meters between the riverbed and the floodplain [130]. Most floodplain areas are more low-lying than the riverbank of the Lower Han River. Once long-lasting rains arrive (just as in the 2010 flood event), the flood water is hard to discharge and many parts of the floodplain can become water-impregnated, leading to poor productivity. Meanwhile, in previous experimental research, crop yield has been identified to be reduced linearly with the duration of waterlogging [41,42,131]. Thus, the flow duration can be considered as the most influential flood parameter in predicting damage to crop production in the Han River Basin.

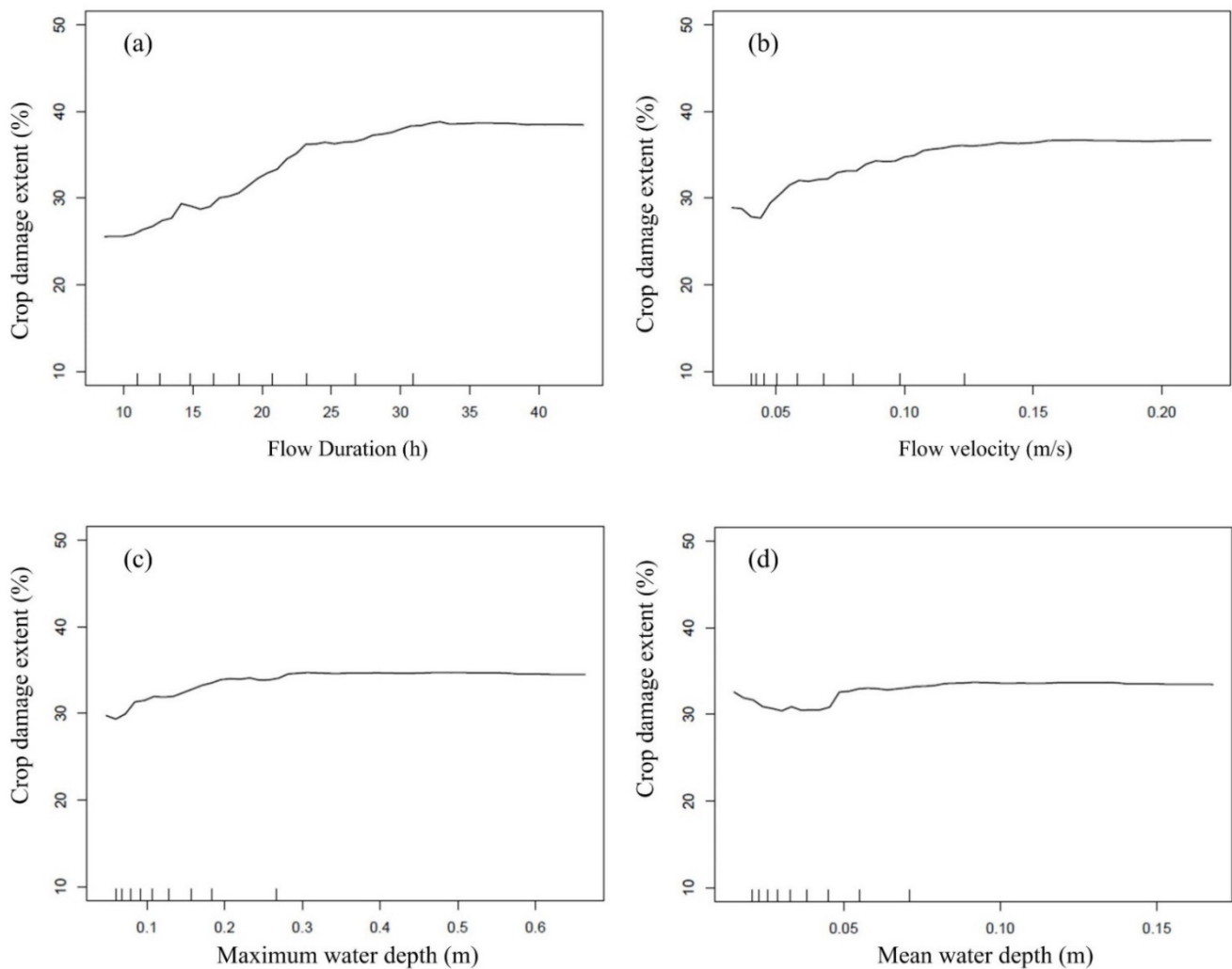


Figure 7. The relationship between (a) flow duration, (b) flow velocity, (c) maximum water depth, (d) mean water depth and crop damage extent detected by the random forest model. The predictors are sorted by their importance.

4. Discussion

The flood parameters can be adopted to construct “loss functions” for agriculture. The parameters include water depth, water duration, flow velocity, water salinity, deposits, and contamination by pollution [132]. The flood parameter most frequently adopted in “loss functions” is water depth, and this is generally the only parameter used to evaluate damage to plant material [14,115,117–119,133–136]. However, flood duration [127,129,137–139] and flow velocity [120,129,139] are not always taken into account in classical “loss functions”. In fact, flood simulations, including the analysis of flood duration and flow velocity, should be employed in advance if “loss functions” which take into account this parameter are suitable for the floods and areas needing to be assessed. For example, the necessity of

considering flow velocity depends on the type of flood occurring. If a flood event is a flash flood, it is extremely important to take into account this parameter [35]. Yet, in the Han River Basin, for example, the most notable features are a flattened floodplain and a long duration of excessive rainfall; flood duration is important in constructing appropriate “loss functions” for local agriculture. Moreover, crop yield losses can also be impacted by the crop types planted during the flood period [38]. Rice is the most abundant crop in the Han River Basin, and it can form longitudinal interconnections for gas to realize the internal aeration of shoots and roots, leading to it having a good tolerance to excess water stress [140].

Since the flow velocity and flood duration can only be obtained from 2D hydraulic flood modeling [68], which lead to a limited number of studies utilized flow velocity and flood duration in crop loss assessment. The research that calculated the flood characteristics by 2D hydraulic models were listed in Table 2 for a quantitative literature review. We ranked the flood characteristics, flood types, crop types, and flood simulation models of related research. Table 2 shows that the importance rank of flood duration, flow velocity, and water depth varies greatly over different watersheds, flood types, and crop types. Thus, more research is needed to determine the relationship between flood parameters and crop yield losses in more basins.

Table 2. The importance rank of Flood Duration (FD), Flow Velocity (FV), and Water Depth (WD) calculated by 2D hydraulic models in crop yield loss related studies.

Location	Flood Duration	Flow Velocity	Water Depth	Parameter Importance Rank	Flood Type	Crop Type	Flood Simulation Model.
Greece [120] 130 km ²	×	✓	✓	WD > FV	flash flood	Fruit trees, olive trees, tomatoes and green vegetables.	Mike Flood.
Germany [137] 838 km ²	✓	✓	×	Did not mention.	flash flood	Wheat, barley, and corn.	2D hydrodynamic model.
Mexico [139] 649 km ²	✓	✓	✓	FD > FV	Long-duration	Corn.	Mike 21.
Indonesia [129] 16,000 km ²	✓	✓	✓	WD > FV, WD > FD	Long-duration	Rice.	2D hydraulic model.
China [35] 2953 km ²	✓	✓	✓	FV > WD > FD	Long-duration	Soybean, corn, and rice.	2D hydraulic model.
China 159,000 km ² This research	✓	✓	✓	FD > FV > WD	Long-duration	Multiple crops.	2D hydraulic model.

5. Conclusions

In this work, a comprehensive and spatially explicit risk evaluation framework was developed to investigate how floods impact crop production. A simple and effective index was proposed for detecting flood disturbances in crop production against the backdrop of natural fluctuations in long-duration floods and multi-cropping agricultural systems on a pixel-by-pixel basis. A coupled hydrological and 2D hydraulic model was employed to simulate flood flows in order to derive flood inundation patterns and processes over the whole basin. The evaluation framework was tested in the MLYRB and the assessment results indicated the following: (1) the new disturbance detection index is capable of acquiring a spatially explicit crop damage map, which is verified by the governmental statistics and related reports and coordinated with the spatial characteristics of river floods;

(2) the coupled hydrological and 2D hydraulic model, with the help of GPU parallel computing, can provide enough meaningful detail on time-varying and grid-based flood depths, velocities, and durations over the whole basin, and the simulated surface water areas show a favorable level of agreement with the HJ imagery; (3) flood duration and flow velocity are positively correlated with crop damage extent, as expected, with flood duration being the most important variable in predicting crop damage extent in the MLYRB.

Author Contributions: Conceptualization, H.C.; methodology, H.C.; literature search, X.W.; resources, X.W. and Z.L.; writing—original draft preparation, H.C.; writing—review and editing, X.W.; funding acquisition, H.C. and X.W. All authors have read and agreed to the published version of the manuscript.

Funding: This work was supported by the National Basic Research Program of China (2015CB458900), the National Science Foundation of China (51721006), Major Science and Technology Program for Water Pollution Control and Treatment of China(2014ZX07203-008), and the open fund of the Ministry of Education Laboratory for Earth Surface Processes.

Institutional Review Board Statement: Not applicable.

Conflicts of Interest: The authors declare no conflict of interest.

References

- Schmidhuber, J.; Tubiello, F.N. Global food security under climate change. *Proc. Natl. Acad. Sci. USA* **2007**, *104*, 19703–19708. [[CrossRef](#)]
- Vervuren, P.; Blom, C.W.P.M.; De-Kroon, H. Extreme flooding events on the Rhine and the survival and distribution of riparian plant species. *J. Ecol.* **2003**, *91*, 135–146. [[CrossRef](#)]
- Youssef, M.S.; Mira, M.M.; Renault, S.; Hill, R.D.; Stasolla, C. Phytoglobulin expression influences soil flooding response of corn plants. *Ann. Bot.* **2016**, *118*, 919–931. [[CrossRef](#)]
- Sun, L.; Chen, S.; Chao, L.; Sun, T. Effects of flooding on changes in Eh, pH and speciation of cadmium and lead in contaminated soil. *Bull. Environ. Contam. Toxicol.* **2007**, *79*, 514–518. [[CrossRef](#)]
- Urban, D.W.; Roberts, M.J.; Schlenker, W.; Lobell, D.B. The effects of extremely wet planting conditions on maize and soybean yields. *Clim. Change* **2015**, *130*, 247–260. [[CrossRef](#)]
- Christopher, B.F.; Vicente, B.; Thomas, F.S.; Qin, D. *Managing the Risks of Extreme Events and Disasters to Advance Climate Change Adaptation*; Cambridge University Press: Cambridge, UK, 2012; pp. 109–230.
- Blöschl, G.; Hall, J.; Parajka, J.; Perdigão, R.A.P.; Merz, B.; Arheimer, B.; Aronica, G.T.; Bilibashi, A.; Bonacci, O.; Borga, M.; et al. Changing climate shifts timing of European floods. *Science* **2017**, *357*, 588–590. [[CrossRef](#)]
- Jiabo, Y.; Shenglian, G.; Pierre, G.; Sylvia, C. Does the Hook Structure Constrain Future Flood Intensification Under Anthropogenic Climate Warming? *Water Resour. Res.* **2021**, *57*, 2020.
- Liu, J.; Shi, Z.W. Quantifying land-use change impacts on the dynamic evolution of flood vulnerability. *Land Use Policy* **2017**, *65*, 198–210. [[CrossRef](#)]
- Liu, X.; Chen, L.; Zhu, Y.; Singh, V.P.; Qu, G.; Guo, X. Multi-objective reservoir operation during flood season considering spillway optimization. *J. Hydrol.* **2017**, *552*, 554–563. [[CrossRef](#)]
- Zhang, Q.; Xu, C.Y.; Zhang, Z.; Chen, Y.D.; Liu, C.L.; Lin, H. Spatial and temporal variability of precipitation maxima during 1960–2005 in the Yangtze River basin and possible association with large-scale circulation. *J. Hydrol.* **2008**, *353*, 215–227. [[CrossRef](#)]
- Yin, H.; Li, C. Human impact on floods and flood disasters on the Yangtze River. *Geomorphology* **2001**, *41*, 105–109. [[CrossRef](#)]
- Chen, Z.; Li, J.; Shen, H.; Wang, Z. Yangtze River of China: Historical analysis of discharge variability and sediment flux. *Geomorphology* **2001**, *41*, 77–91. [[CrossRef](#)]
- Yu, F.; Chen, Z.; Ren, X.; Yang, G. Analysis of historical floods on the Yangtze River, China: Characteristics and explanations. *Geomorphology* **2009**, *113*, 210–216. [[CrossRef](#)]
- Jiang, L.; An, P. Temporal and spatial distribution and grain risk assessment of natural disasters in China. *J. Catastrophology* **2011**, *26*, 48–53. (In Chinese)
- Su, B.; Xiao, B.; Zhu, D.; Jiang, T. Trends in frequency of precipitation extremes in the Yangtze River basin, China: 1960–2003. *Hydrol. Sci. J.* **2005**, *50*, 479–492.
- Zhang, Q.; Peng, J.; Xu, C.Y.; Singh, V.P. Spatiotemporal variations of precipitation regimes across Yangtze River Basin, China. *Theor. Appl. Climatol.* **2014**, *115*, 703–712. [[CrossRef](#)]
- Hu, M.; Dong, M.; Tian, X.; Wang, L.; Jiang, Y. Trends in Different Grades of Precipitation over the Yangtze River Basin from 1960 to 2017. *Atmosphere* **2021**, *12*, 413. [[CrossRef](#)]
- Li, X.; Zhang, K.; Gu, P.; Feng, H.; Yin, Y.; Chen, W.; Cheng, B. Changes in precipitation extremes in the Yangtze River Basin during 1960–2019 and the association with global warming, ENSO, and local effects. *Sci. Total Environ.* **2021**, *760*, 144244. [[CrossRef](#)]

20. Su, B.; Kundzewicz, Z.W.; Tong, J. Simulation of extreme precipitation over the Yangtze River basin using Wakeby distribution. *Theor. Appl. Climatol.* **2009**, *96*, 209–219. [[CrossRef](#)]
21. Wu, Y.; Wu, S.Y.; Wen, J.; Tagle, F.; Xu, M.; Tan, J. Future Changes in Mean and Extreme Monsoon Precipitation in the Middle and Lower Yangtze River Basin, China, in the CMIP5 Models. *J. Hydrometeorol.* **2016**, *17*, 2785–2797. [[CrossRef](#)]
22. Zhang, Z.; Zhang, Q.; Xu, C.; Liu, C.; Jiang, T. Atmospheric moisture budget and floods in the Yangtze River basin, china. *Theor. Appl. Climatol.* **2009**, *95*, 331–340. [[CrossRef](#)]
23. Yin, R.S.; Xiang, Q.; Xu, J.T.; Deng, X.Z.; Yin, R. Modeling the driving forces of the land use and land cover changes along the upper Yangtze River of China. *Environ. Manag.* **2010**, *45*, 454–465. [[CrossRef](#)]
24. Cong, X.; Xin, H.; Mu, H.; Wei, Y. Impacts of land-use changes on the lakes across the Yangtze floodplain in china. *Environ. Sci. Technol.* **2017**, *51*, 3669.
25. Nakayama, T.; Watanabe, M. Role of flood storage ability of lakes in the Changjiang River catchment. *Glob. Planet. Change* **2008**, *63*, 9–22. [[CrossRef](#)]
26. Du, Y.; Xue, H.P.; Wu, S.J.; Ling, F.; Xiao, F.; Wei, X.H. Lake area changes in the middle Yangtze region of China over the 20th century. *J. Environ. Manag.* **2011**, *92*, 1248–1255. [[CrossRef](#)]
27. Zhang, Q.; Liu, C.; Xu, C.Y.; Xu, Y.; Jiang, T. Observed trends of annual maximum water level and streamflow during past 130 years in the Yangtze River basin, china. *J. Hydrol.* **2006**, *324*, 255–265. [[CrossRef](#)]
28. Nakayama, T.; Shankman, D. Impact of the Three-Gorges Dam and water transfer project on Changjiang floods. *Glob. Planet. Change* **2013**, *100*, 38–50. [[CrossRef](#)]
29. Meng, L.; Wang, C.; Zhang, J. Heat injury risk assessment for single-cropping rice in the middle and lower reaches of the Yangtze River under climate change. *J. Meteorol. Res.* **2016**, *30*, 426–443. [[CrossRef](#)]
30. Lesk, C.; Rowhani, P.; Ramankutty, N. Influence of extreme weather disasters on global crop production. *Nature* **2016**, *529*, 84–87. [[CrossRef](#)]
31. Lee, K.S.; Lee, S.I. Assessment of post-flooding conditions of rice fields with multi-temporal satellite SAR data. *Int. J. Remote Sens.* **2003**, *24*, 3457–3465. [[CrossRef](#)]
32. Pantaleoni, E.; Engel, B.A.; Johannsen, C.J. Identifying agricultural flood damage using Landsat imagery. *Precis. Agric.* **2007**, *8*, 27–36. [[CrossRef](#)]
33. Džubáková, K.; Molnar, P.; Schindler, K.; Trizna, M. Monitoring of riparian vegetation response to flood disturbances using terrestrial photography. *Hydrol. Earth Syst. Sci.* **2015**, *19*, 195–208. [[CrossRef](#)]
34. Shrestha, R.; Di, L.; Eugene, G.Y.; Kang, L.; Shao, Y.Z.; Bai, Y.Q. Regression model to estimate flood impact on corn yield using MODIS NDVI and USDA cropland data layer. *J. Integr. Agric.* **2017**, *16*, 398–407. [[CrossRef](#)]
35. Chen, H.; Liang, Z.; Liu, Y.; Liang, Q.; Xie, S. Integrated remote sensing imagery and two-dimensional hydraulic modeling approach for impact evaluation of flood on crop yields. *J. Hydrol.* **2017**, *553*, 262–275. [[CrossRef](#)]
36. Zhang, X.; Friedl, M.A.; Schaaf, C.B.; Strahler, A.H.; Hodges, J.C.F.; Gao, F.; Reed, B.C.; Huete, A. Monitoring vegetation phenology using MODIS. *Remote Sens. Environ.* **2003**, *84*, 471–475. [[CrossRef](#)]
37. Sakamoto, T.; Yokozawa, M.; Toritani, H.; Shibayama, M.; Ishitsuka, N.; Ohno, H. A crop phenology detection method using time-series MODIS data. *Remote Sens. Environ.* **2005**, *96*, 366–374. [[CrossRef](#)]
38. Chen, H.; Liang, Q.; Liang, Z.; Liu, Y.; Xie, S. Remote-sensing disturbance detection index to identify spatio-temporal varying flood impact on crop production. *Agric. For. Meteorol.* **2019**, *269*, 180–191. [[CrossRef](#)]
39. Samuels, P.; Klijn, F.; Dijkman, J. An analysis of the current practice of policies on river flood risk management in different countries. *Irrig. Drain.* **2006**, *55*, S141–S150. [[CrossRef](#)]
40. Dinh, Q.; Balica, S.; Popescu, I.; Jonoski, A. Climate change impact on flood hazard, vulnerability and risk of the Long Xuyen Quadrangle in the Mekong Delta. *Int. J. River Basin Manag.* **2012**, *10*, 103–120. [[CrossRef](#)]
41. Marti, J.; Savin, R.; Slafer, G.A. Wheat yield as affected by length of exposure to waterlogging during stem elongation. *J. Agron. Crop Sci.* **2015**, *201*, 473–486. [[CrossRef](#)]
42. Kaur, G.; Zurweller, B.A.; Nelson, K.A.; Motavalli, P.P.; Dudenhoefter, C.J. Soil waterlogging and nitrogen fertilizer management effects on corn and soybean yields. *Agron. J.* **2017**, *109*, 97–106. [[CrossRef](#)]
43. Ploschuk, R.A.; Daniel, J.M.; Timothy, D.C.; Striker, G.G. Waterlogging differentially affects yield and its components in wheat, barley, rapeseed and field pea depending on the timing of occurrence. *J. Agron. Crop Sci.* **2020**, *206*, 363–375. [[CrossRef](#)]
44. Meng, Y.; Yu, S.; Yu, Y.; Jiang, L. Flooding depth and duration concomitantly influence the growth traits and yield of rice. *Irrig. Drain.* **2021**, *9*, 94–107. [[CrossRef](#)]
45. Yang, J.; Huo, Z.; Wu, L.; Wang, T.; Zhang, G. Indicator-based evaluation of spatiotemporal characteristics of rice flood in southwest china. *Agric. Ecosyst. Environ.* **2016**, *230*, 221–230. [[CrossRef](#)]
46. Li, S.; Tompkins, A.M.; Lin, E.; Ju, H. Simulating the impact of flooding on wheat yield—Case study in East China. *Agric. For. Meteorol.* **2016**, *216*, 221–231. [[CrossRef](#)]
47. Chipanshi, A.; Zhang, Y.; Kouadio, L.; Newlands, N.; Davidson, A.; Hill, H.; Warren, R.; Qian, B.; Daneshfar, B.; Bedard, F.; et al. Evaluation of the integrated Canadian crop yield forecaster (ICCYF) model for in-season prediction of crop yield across the Canadian agricultural landscape. *Agric. For. Meteorol.* **2015**, *206*, 137–150. [[CrossRef](#)]
48. Biancamaria, S.; Bates, P.D.; Boone, A.; Mognard, N.M. Large-scale coupled hydrologic and hydraulic modelling of the Ob river in Siberia. *J. Hydrol.* **2009**, *379*, 136–150. [[CrossRef](#)]

49. Caviedes-Voullième, D.; García-Navarro, P.; Murillo, J. Influence of mesh structure on 2D full shallow water equations and SCS Curve Number simulation of rainfall/runoff events. *J. Hydrol.* **2012**, *448–449*, 39–59. [[CrossRef](#)]
50. Cea, M.; Rodriguez, M. Two-dimensional coupled distributed hydrologic–hydraulic model simulation on watershed. *Pure Appl. Geophys.* **2016**, *173*, 909–922. [[CrossRef](#)]
51. Fernández-Pato, J.; Caviedes-Voullième, D.; García-Navarro, P. Rainfall/runoff simulation with 2d full shallow water equations: Sensitivity analysis and calibration of infiltration parameters. *J. Hydrol.* **2016**, *536*, 496–513. [[CrossRef](#)]
52. Liu, Z.; Merwade, V.; Jafarzadegan, K. Investigating the role of model structure and surface roughness in generating flood inundation extents using one-and two-dimensional hydraulic models. *J. Flood Risk Manag.* **2019**, *12*, e12347. [[CrossRef](#)]
53. Shen, D.; Qian, T.; Xia, Y.; Zhang, Y.; Wang, J. Micro-scale Flood Hazard Assessment Based on Catastrophe Theory and an Integrated 2-D Hydraulic Model: A Case Study of Gongshuangcha Detention Basin in Dongting Lake Area, China. *ISPRS Int. J. Geo-Inf.* **2020**, *9*, 206. [[CrossRef](#)]
54. Yamazaki, D.; Kanae, S.; Kim, H.; Oki, T. A physically based description of floodplain inundation dynamics in a global river routing model. *Water Resour. Res.* **2011**, *47*, W04501. [[CrossRef](#)]
55. Schumann, J.P.; Neal, J.C.; Voisin, N.; Andreadis, K.M.; Pappenberger, F.; Phanthuwongpakdee, N.; Hall, A.C.; Bates, P.D. A first large-scale flood inundation forecasting model. *Water Resour. Res.* **2013**, *49*, 6248–6257. [[CrossRef](#)]
56. Kalyanapu, A.J.; Shankar, S.; Pardyjak, E.R.; Judi, D.R.; Burian, S.J. Assessment of GPU computational enhancement to a 2D flood model. *Environ. Model. Softw.* **2011**, *26*, 1009–1016. [[CrossRef](#)]
57. Vacondio, R.; Dal Palù, A.; Ferrari, A.; Mignosa, P.; Aureli, F.; Dazzi, S. A non-uniform efficient grid type for GPU-parallel Shallow Water Equations models. *Environ. Model. Softw.* **2017**, *88*, 119–137. [[CrossRef](#)]
58. Wu, Q.; Chen, Y.; Wilson, J.; Liu, X.; Li, H. An effective parallelization algorithm for DEM generalization based on CUDA. *Environ. Model. Softw.* **2019**, *114*, 64–74. [[CrossRef](#)]
59. Morales-Hernández, M.; Sharif, B.; Alfred, J.K.; Sheikh, K.G.; Tigstu, T.D.; Gangrade, S.; Kao, S.; Matthew, R.N.; Katherine, J.E. TRITON: A Multi-GPU open source 2D hydrodynamic flood model. *Environ. Model. Softw.* **2021**, *141*, 105034. [[CrossRef](#)]
60. Carlotto, T.; Chaffe, P.L.B.; Santos, C.I.D.; Lee, S. SW2D-GPU: A two-dimensional shallow water model accelerated by GPGPU. *Environ. Model. Softw.* **2021**, *145*, 105205. [[CrossRef](#)]
61. Armstrong, W. Aeration in higher plants. *Adv. Bot. Res.* **1980**, *7*, 225–332.
62. Collaku, A.; Harrison, S.A. Losses in wheat due to waterlogging. *Crop Sci.* **2002**, *42*, 444–450. [[CrossRef](#)]
63. Kaur, G.; Zurweller, B.; Motavalli, P.P.; Nelson, K.A. Screening Corn Hybrids for Soil Waterlogging Tolerance at an Early Growth Stage. *Agriculture* **2019**, *9*, 33. [[CrossRef](#)]
64. Gautam, P.; Lal, B.; Raja, R.; Tripathi, R.; Shahid, M.; Baig, M.J.; Puree, C.; Mohanty, S.; Nayak, A.K. Effect of simulated flash flooding on rice and its recovery after flooding with nutrient management strategies. *Ecol. Eng.* **2015**, *77*, 250–256. [[CrossRef](#)]
65. Ding, J.; Liang, P.; Guo, D.; Liu, D.; Yin, M.; Zhu, M.; Li, C.; Zhu, X.; Guo, W. Remedial Application of Urea Eliminates Yield Losses in Wheat Waterlogged during Stem Elongation. *Agriculture* **2020**, *10*, 23. [[CrossRef](#)]
66. Ciancio, N.; Daniel, J.M.; Striker, G.G.; Abeledo, L.G. Plant growth rate after, and not during, waterlogging better correlates to yield responses in wheat and barley. *J. Agron. Crop Sci.* **2021**, *207*, 304–316. [[CrossRef](#)]
67. Zhang, X.; Zhang, Q. Monitoring interannual variation in global crop yield using long-term AVHRR and MODIS observations. *ISPRS J. Photogramm. Remote Sens.* **2016**, *114*, 191–205. [[CrossRef](#)]
68. Rahman, M.S.; Di, L. A Systematic Review on Case Studies of Remote-Sensing-Based Flood Crop Loss Assessment. *Agriculture* **2020**, *10*, 131. [[CrossRef](#)]
69. Benedetti, R.; Rossini, P. On the use of NDVI profiles as a tool for agricultural statistics: The case study of wheat yield estimate and forecast in Emilia Romagna. *Remote Sens. Environ.* **1993**, *45*, 311–326. [[CrossRef](#)]
70. Funk, C.; Budde, M.E. Phenologically-tuned MODIS NDVI-based production anomaly estimates for Zimbabwe. *Remote Sens. Environ.* **2009**, *113*, 115–125. [[CrossRef](#)]
71. Esquerdo, J.C.D.M.; Zullo Júnior, J.; Antunes, J.F.G. Use of NDVI/AVHRR time-series profiles for soybean crop monitoring in Brazil. *Int. J. Remote Sens.* **2011**, *32*, 3711–3727. [[CrossRef](#)]
72. Son, N.T.; Chen, C.F.; Chen, C.R.; Minh, V.Q.; Trung, N.H. A comparative analysis of multitemporal MODIS EVI and NDVI data for large-scale rice yield estimation. *Agric. For. Meteorol.* **2014**, *197*, 52–64. [[CrossRef](#)]
73. Bernardes, T.; Moreira, M.A.; Adami, M.; Giarolla, A. Monitoring biennial bearing effect on coffee yield using MODIS remote sensing imagery. *Remote Sens.* **2012**, *4*, 3760–3763. [[CrossRef](#)]
74. Zhang, J.; Feng, L.; Yao, F. Improved maize cultivated area estimation over a large scale combining MODIS–EVI time series data and crop phenological information. *ISPRS J. Photogramm. Remote Sens.* **2014**, *94*, 102–113. [[CrossRef](#)]
75. Huete, A.; Didan, K.; Miura, T.; Rodriguez, E.P.; Gao, X.; Ferreira, L.G. Overview of the radiometric and biophysical performance of the MODIS vegetation indices. *Remote Sens. Environ.* **2002**, *83*, 195–213. [[CrossRef](#)]
76. Rocha, A.V.; Shaver, G.R. Advantages of a two band EVI calculated from solar and photosynthetically active radiation fluxes. *Agric. For. Meteorol.* **2009**, *149*, 1560–1563. [[CrossRef](#)]
77. Mildrexler, D.J.; Zhao, M.; Running, S.W. Testing a MODIS global disturbance index across North America. *Remote Sens. Environ.* **2009**, *113*, 2103–2117. [[CrossRef](#)]

78. Woodward, D.; Hawkings, R.; Hjelmfelt, A.; Van Mullen, J.; Quan, Q. Curve Number Method: Origins, Applications and Limitations. In Proceedings of the US Geological Survey Advisory Committee on Water Information—Second Federal Interagency Hydrologic Modeling Conference, Las Vegas, NV, USA, 28 July–1 August 2002.
79. Bartlett, M.S.; Parolari, A.J.; McDonnell, J.J.; Porporato, A. Beyond the SCS-CN method: A theoretical framework for spatially lumped rainfall-runoff response. *Water Resour. Res.* **2016**, *52*, 4608–4627. [[CrossRef](#)]
80. Mishra, S.K.; Singh, V.P. *Soil Conservation Service Curve Number (SCS-CN) Methodology (Volume 42)*, 1st ed.; Kluwer Academic Publisher: New York, NY, USA, 2003; pp. 88–108.
81. Liang, Q.; Marche, F. Numerical resolution of well-balanced shallow water equations with complex source terms. *Adv. Water Resour.* **2009**, *32*, 873–884. [[CrossRef](#)]
82. Song, L.; Zhou, J.; Guo, J.; Zou, Q.; Liu, Y. A robust well-balanced finite volume model for shallow water flows with wetting and drying over irregular terrain. *Adv. Water Resour.* **2011**, *34*, 915–932. [[CrossRef](#)]
83. Hou, J.; Liang, Q.; Zhang, H.; Hinkelmann, R. An efficient unstructured MUSCL scheme for solving the 2D shallow water equations. *Environ. Model. Softw.* **2015**, *66*, 131–152. [[CrossRef](#)]
84. Xia, X.; Liang, Q.; Ming, X.; Hou, J. An efficient and stable hydrodynamic model with novel source term discretization schemes for overland flow and flood simulations. *Water Resour. Res.* **2017**, *53*, 3730–3759. [[CrossRef](#)]
85. Su, B.; Huang, H.; Zhu, W. An urban pluvial flood simulation model based on diffusive wave approximation of shallow water equations. *Hydrol. Res.* **2019**, *50*, 138–154. [[CrossRef](#)]
86. Pilar, G.; Javier, M.; Fernández-Pato, J.; Isabel, E.; Mario, M. The shallow water equations and their application to realistic cases. *Environ. Fluid Mech.* **2019**, *19*, 1235–1252.
87. Vreugdenhil, C.B. *Numerical Methods for Shallow-Water Flow (Volume 13)*, 1st ed.; Kluwer Academic Publisher: New York, NY, USA, 1994; pp. 15–41.
88. Dehghan, M.; Abbaszadeh, M.; Dehghan, M.; Abbaszadeh, M. The use of proper orthogonal decomposition (POD) meshless RBF-FD technique to simulate the shallow water equations. *J. Comput. Phys.* **2017**, *351*, 478–510. [[CrossRef](#)]
89. Francesca, A.; Federico, P.; Vacondio, R.; Susanna, D.; Alessia, F. A GPU-Accelerated Shallow-Water Scheme for Surface Runoff Simulations. *Water* **2020**, *12*, 637.
90. NVIDIA CUDA. NVIDIA CUDA C++ Programming Guide v11.4. 2021. Available online: https://docs.nvidia.com/cuda/pdf/CUDA_C_Programming_Guide.pdf (accessed on 24 January 2022).
91. Schumann, G.J.P.; Bates, P.D.; Neal, J.C.; Andreadis, K.M. Technology: Fight floods on a global scale. *Nature* **2014**, *507*, 169. [[CrossRef](#)]
92. Yamazaki, D.; Ikeshima, D.; Tawatari, R.; Yamaguchi, T.; O’Loughlin, F.; Neal, J.C. A high-accuracy map of global terrain elevations. *Geophys. Res. Lett.* **2017**, *44*, 5844–5853. [[CrossRef](#)]
93. Chen, H.L.; Liang, Q.H.; Liu, Y.; Xie, S. Hydraulic correction method (HCM) to enhance the efficiency of SRTM DEM in flood modeling. *J. Hydrol.* **2018**, *559*, 56–70. [[CrossRef](#)]
94. Song, S.; He, R.; Shi, Z.; Zhang, W. Variable Importance Measure System Based on Advanced Random Forest. *CMES-Comput. Modeling Eng. Sci.* **2021**, *128*, 65–85. [[CrossRef](#)]
95. Breiman, L. Random forests. *Mach. Learn.* **2001**, *45*, 5–32. [[CrossRef](#)]
96. Welling, S.H.; Refsgaard, H.H.F.; Brockhoff, P.B.; Clemmensen, L.H. Forest Floor Visualizations of Random Forests. 2016. Available online: <https://arxiv.org/abs/1605.09196> (accessed on 4 July 2016).
97. Liaw, A.; Wiener, M. Classification and Regression by random Forest. *R News* **2002**, *2*, 18–22.
98. R Core Team. *A Language and Environment for Statistical Computing*; R Foundation for Statistical Computing: Vienna, Austria, 2015; Available online: <http://www.R-project.org/> (accessed on 24 January 2022).
99. Ding, Y.; Wang, W.; Song, R.; Shao, Q.; Jiao, X.; Xing, W. Modeling spatial and temporal variability of the impact of climate change on rice irrigation water requirements in the middle and lower reaches of the Yangtze River, China. *Agric. Water Manag.* **2017**, *193*, 89–101. [[CrossRef](#)]
100. Sun, Z.; Zhu, X.; Pan, Y.; Zhang, J. Assessing Terrestrial Water Storage and Flood Potential Using GRACE Data in the Yangtze River Basin, China. *Remote Sens.* **2017**, *9*, 1011. [[CrossRef](#)]
101. Chinese Office of State Flood Control and Drought Relief Headquarters. Flood disaster of China in 2010. *China Flood Drought Manag.* **2011**, *21*, 1–3.
102. Li, S.; Zhang, Q. Geochemistry of the upper Han River basin, China: 2: Seasonal variations in major ion compositions and contribution of precipitation chemistry to the dissolved load. *J. Hazard. Mater.* **2009**, *170*, 605–611. [[CrossRef](#)]
103. Liu, W.; Liu, G.; Zhang, Q. Influence of vegetation characteristics on soil denitrification in shoreline wetlands of the Danjiangkou Reservoir in China. *Clean-Soil Air Water* **2011**, *39*, 109–115. [[CrossRef](#)]
104. Huete, A.; Didan, K.; Leeuwen, W.V.; Miura, T.; Glenn, E. MODIS Vegetation Indices. In *Land Remote Sensing and Global Environmental Change*; Ramachandran, B., Christopher, O.J., Michael, J.A., Eds.; Springer: New York, NY, USA; Dordrecht, The Netherlands; Heidelberg, Germany; London, UK, 2011; Volume 11, pp. 579–602.
105. Ticehurst, C.; Guerschman, J.P.; Chen, Y. The strengths and limitations in using the daily MODIS open water likelihood algorithm for identifying flood events. *Remote Sens.* **2014**, *6*, 11791–11809. [[CrossRef](#)]
106. Huete, A.; Justice, C.O.; Van Leeuwen, W. MODIS Vegetation Index (MOD13): Algorithm Theoretical Basis Document. 2011. Available online: http://modis.gsfc.nasa.gov/data/atbd/atbd_mod13.pdf (accessed on 8 February 2011).

107. Arino, O.; Perez, J.J.R.; Kalogirou, V.; Bontemps, S.; Defourny, P.; Van Bogaert, E. Global Land Cover Map for 2009 (GlobCover 2009). European Space Agency (ESA) & Université Catholique de Louvain (UCL), PANGAEA. 2012. Available online: <https://doi.org/10.1594/PANGAEA.787668> (accessed on 24 January 2022). [CrossRef]
108. Nachtergaele, F.O.; Velthuisen, V.L.; Batjes, N.H.; Dijkshoorn, J.A.; van Engelen, V.W.P.; Fischer, G.; Jones, A.; Montanarella, L.; Petri, M.; Prieler, S.; et al. Harmonized World Soil Database (Version 1.2). 2012. Available online: <https://research.wur.nl/en/publications/harmonized-world-soil-database-version-12> (accessed on 24 January 2022).
109. Lehner, B.; Verdin, K.; Jarvis, A. New global hydrography derived from spaceborne elevation data. *Eos Trans. Am. Geophys. Union* **2008**, *89*, 93–94. [CrossRef]
110. Zhang, Q.; Gu, X.; Singh, V.P.; Liu, L.; Kong, D. Flood-induced agricultural loss across China and impacts from climate indices. *Glob. Planet. Change* **2016**, *139*, 31–43. [CrossRef]
111. Tehrany, M.S.; Pradhan, B.; Mansor, S.; Ahmad, N. Flood susceptibility assessment using GIS-based support vector machine model with different kernel types. *Catena* **2015**, *125*, 91–101. [CrossRef]
112. Kazakis, N.; Kougias, I.; Patsialis, T. Assessment of flood hazard areas at a regional scale using an index-based approach and Analytical Hierarchy Process: Application in Rhodope–Evros region, Greece. *Sci. Total Environ.* **2015**, *538*, 555–563. [CrossRef] [PubMed]
113. Samela, C.; Troy, T.J.; Manfreda, S. Geomorphic classifiers for flood-prone areas delineation for data-scarce environments. *Adv. Water Resour.* **2017**, *102*, 13–28. [CrossRef]
114. Tang, Z.; Yi, S.; Wang, C.; Xiao, Y. Incorporating probabilistic approach into local multi-criteria decision analysis for flood susceptibility assessment. *Stoch. Environ. Res. Risk Assess.* **2018**, *32*, 701–714. [CrossRef]
115. Chau, V.N.; Cassells, S.; Holland, J. Economic impact upon agricultural production from extreme flood events in Quang Nam, central Vietnam. *Nat. Hazards* **2015**, *75*, 1747–1765. [CrossRef]
116. Dao, P.; Liou, Y. Object-based flood mapping and affected rice field estimation with Landsat 8 OLI and MODIS data. *Remote Sens.* **2015**, *7*, 5077–5097. [CrossRef]
117. Sande, C.J.V.D.; Jong, S.M.D.; Roo, A.P.J.D. A segmentation and classification approach of ikonos-2 imagery for land cover mapping to assist flood risk and flood damage assessment. *Int. J. Appl. Earth Obs. Geoinf.* **2003**, *4*, 217–229. [CrossRef]
118. Jonkman, S.N.; Bočkarjova, M.; Kok, M.; Bernardini, P. Integrated hydrodynamic and economic modelling of flood damage in the Netherlands. *Ecol. Econ.* **2008**, *66*, 77–90. [CrossRef]
119. Vozinaki, A.E.K.; Kourgialas, N.N.; Karatzas, G.P. Estimation of agricultural flood loss in the Koiliaris river basin in Crete, Greece. *Eur. Water.* **2012**, *39*, 53–63.
120. Vozinaki, A.E.K.; Karatzas, G.P.; Sibtheros, I.A.; Varouchakis, E.A. An agricultural flash flood loss estimation methodology: The case study of the Koiliaris basin (Greece), February 2003 flood. *Nat. Hazards* **2015**, *79*, 899–920. [CrossRef]
121. Juan, P.; Luis, T. Performance assessment of two-dimensional hydraulic models for generation of flood inundation maps in mountain river basins. *Water Sci. Eng.* **2019**, *12*, 11–18.
122. Jia, D.W.; Zhong, S.Q.; Li, X.; Peng, B. Extracting water information from the HSI data of HJ-1A/B satellite. *Sci. Surv. Mapp.* **2011**, *36*, 128–130.
123. Wang, Q.Y.; Chen, R.X.; Xu, J.; Chen, X.L. Research on methods for extracting water body information from HJ-1A/B data. *Sci. Technol. Eng.* **2012**, *12*, 3051–3056.
124. Liu, H.; Zheng, L.; Jiang, L.; Liao, M.W. Forty-year water body changes in Poyang Lake and the ecological impacts based on Landsat and HJ-1 A/B observations. *J. Hydrol.* **2020**, *589*, 125–161. [CrossRef]
125. Mohammadi, A.; Costelloe, J.F.; Ryu, D. Application of time series of remotely sensed normalized difference water, vegetation and moisture indices in characterizing flood dynamics of large-scale arid zone floodplains. *Remote Sens. Environ.* **2017**, *190*, 70–82. [CrossRef]
126. Singh, D.S.; Prajapati, S.K.; Singh, P.; Singh, K.; Kumar, D. Climatically induced levee break and flood risk management of the Gorakhpur region, Rapti River basin, Ganga Plain, India. *J. Geol. Soc. India* **2015**, *85*, 79–86. [CrossRef]
127. Shrestha, B.B.; Kawasaki, A. Quantitative assessment of flood risk with evaluation of the effectiveness of dam operation for flood control: A case of the Bago River Basin of Myanmar. *Int. J. Disaster Risk Reduct.* **2020**, *50*, 101707. [CrossRef]
128. Brémond, P.; Grelot, F.; Agenais, A.L. Review article: Economic evaluation of flood damage to agriculture—Review and analysis of existing methods. *Nat. Hazards Earth Syst. Sci.* **2013**, *13*, 2493–2512. [CrossRef]
129. Vempi, S.A.H.; Daisuke, K. Developing flood vulnerability curve for rice crop using remote sensing and hydrodynamic modeling. *Int. J. Disaster Risk Reduct.* **2021**, *54*, 102058.
130. Yin, H.; Liu, G.; Pi, J.; Chen, G.; Li, C. On the river–lake relationship of the middle Yangtze reaches. *Geomorphology* **2007**, *85*, 197–207. [CrossRef]
131. Li, X.T.; Yu, C.Z.; Peng, L.C.; Zhang, F.F.; Li, J.; Yan, F.; Dong, Y.; Feng, B.L. How Does the Waterlogging Regime Affect Crop Yield? A Global Meta-Analysis. *Front. Plant Sci.* **2021**, *12*, 634898–634907.
132. McDonald, G.T. Agricultural flood damage assessment: A review and investigation of a simulation method. *Rev. Mark. Agric. Econ.* **1970**, *38*, 105–120.
133. Lacewell, R.D.; Eidman, V.R. A General Model for Evaluating Agricultural Flood Plains. *Am. J. Agric. Econ.* **1972**, *54*, 92–101. [CrossRef]

134. Hoes, O.; Schuurmans, W. Flood standards or risk analyses for polder management in the Netherlands. *Irrig. Drain.* **2006**, *55*, 113–119. [[CrossRef](#)]
135. Lacewell, R.D.; Freeman, R.; Petit, D.; Rister, E.; Sturdivant, A.; Ribera, L.; Zinn, M. Update of Estimated Agricultural Benefits Attributable to Drainage and Flood Control in Willacy County, Texas. Texas Water Resources Institute. 2006. Available online: <https://hdl.handle.net/1969.1/6084> (accessed on 24 January 2022).
136. Dutta, D.; Herath, S.; Musiaka, K. A mathematical model for flood loss estimation. *J. Hydrol.* **2003**, *277*, 24–49. [[CrossRef](#)]
137. Förster, S.; Kuhlmann, B.; Lindenschmidt, K.E.; Bronstert, A.L. Assessing flood risk for a rural detention area. *Nat. Hazards Earth Syst. Sci.* **2008**, *8*, 311–322. [[CrossRef](#)]
138. Kwak, Y.; Shrestha, B.B.; Yorozuya, A.; Sawano, H. Rapid damage assessment of rice crop after large-scale flood in the Cambodian floodplain using temporal spatial data. *IEEE J. Sel. Top. Appl. Earth Obs. Remote Sens.* **2017**, *8*, 3700–3709. [[CrossRef](#)]
139. Vega-Serratos, B.E.; Domínguez-Mor, R.; Posada-Vanegas, G. Seasonal flood risk assessment in agricultural areas. *Tecnol. Cienc. Agua.* **2018**, *9*, 92–127. [[CrossRef](#)]
140. Nishiuchi, S.; Yamauchi, T.; Takahashi, H.; Kotula, L.; Nakazono, M. Mechanisms for coping with submergence and waterlogging in rice. *Rice* **2012**, *5*, 2. [[CrossRef](#)]